Title
Orientation-Dependent Distortion of Lamellae in a Block Copolymer Electrolyte under DC Polarization

Permalink
https://escholarship.org/uc/item/18q2r3v6

Journal
Macromolecules, 54(17)

ISSN
0024-9297

Authors
Galluzzo, Michael D
Grundy, Lorena S
Takacs, Christopher J
et al.

Publication Date
2021-09-14

DOI
10.1021/acs.macromol.1c01295

Peer reviewed

Orientation-Dependent Distortion of Lamellae in a Block Copolymer Electrolyte under Dc Polarization

Michael D. Galluzzo[1,2], *Lorena S. Grundy*[1,3], *Christopher J. Takacs*[4,5], *Chuntian Cao*[4,6], *Hans-Georg Steinrück*[4,5,7], *Sean Fu*[1], *Michael A. Rivas Valadez*[1], *Michael F. Toney*[6], *and Nitash P. Balsara*[1,2,3,8*]

[1] Department of Chemical and Biomolecular Engineering University of California, Berkeley, CA 94720, United States.

[2] Materials Science Division, Lawrence Berkeley National Laboratory, Berkeley, CA 94720, United States.

[3] Joint Center for Energy Storage Research (JCESR), Lawrence Berkeley National Laboratory, Berkeley, CA 94720, United States.

[4] SSRL Materials Science Division, SLAC National Accelerator Laboratory, Menlo Park, CA 94025, United States.

[5] SLAC National Accelerator Laboratory, Joint Center for Energy Storage Research (JCESR), Menlo Park, CA 94025, United States.

[6] Department of Chemical and Biological Engineering and Joint Center for Energy Storage Research (JCESR), University of Colorado, Boulder, Boulder, CO 80309, United States.

[7] Department Chemie, Universität Paderborn, 33098 Paderborn, Germany.

[8] Energy Storage and Distributed Resources Division, Lawrence Berkeley National Laboratory, Berkeley, CA 94720, United States.

AUTHOR INFORMATION

Corresponding Author

* Correspondence to: nbalsara@berkeley.edu

ABSTRACT

Lithium-salt-doped block copolymers have the potential to serve as solid electrolytes in rechargeable batteries with lithium metal anodes. In this work, we use small angle X-ray scattering (SAXS) to study the structure of polystyrene-block-poly(ethylene oxide) doped with bis-(trifluoromethylsulfonyl)amine lithium salt (LiTFSI) during dc polarization experiments in lithium-lithium symmetric cells. The block copolymer studied is nearly symmetric in composition, has a total molecular weight of 39 kg mol^{-1}, and it exhibits a lamellar morphology at all studied salt concentrations. When ionic current is passed through the electrolyte, a salt concentration gradient forms which induces a spatial gradient in the domain spacing, d. The dependence of d on distance from the positive electrode, x, was determined experimentally by scanning the incident X-ray beam from one lithium electrode to the other. By studying the 2D SAXS patterns as a function of azimuthal scattering angle, we find that lamellae with PS-PEO interfaces oriented perpendicular to the flow of ionic current (LAM) swell and contract to a greater degree than those with interfaces oriented parallel to the current direction ($LAM_{¿∨¿¿}$). While domains with the LAM do not provide direct conducting pathways between the electrodes, our analysis suggests they play an important role in establishing the salt concentration gradient necessary for sustaining large ionic current through greater expansion and contraction.

For Table of Contents use only
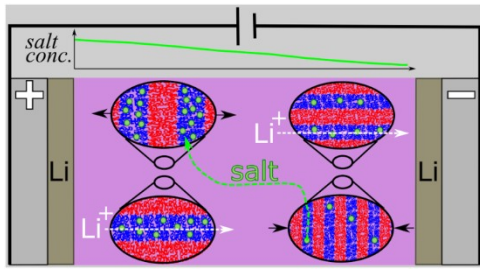
MAIN TEXT

Introduction

Solid-state lithium metal batteries are an attractive alternative to standard lithium-ion batteries as they offer improved energy density.[1] Lithium metal has the highest theoretical specific capacity (3.86 Ah g^{-1}) of any anode material for lithium-based batteries.[2,3] Nanostructured block copolymer electrolytes present one approach for enabling solid-state lithium metal batteries.[4] Polymer-based lithium metal batteries have had limited commercial success for many reasons including limited electrolyte conductivity, the need to establish new manufacturing protocols, and issues related to the reactive and pyrophoric nature of lithium metal.[5]

The purpose of this paper is to shed light on the nature of ion transport in nanostructured block copolymers under dc polarization. Prior to polarization, the salt ions are uniformly distributed in all block copolymer domains. In systems wherein both the cation and anion are mobile and the cation transference number with respect to the solvent velocity, $t_{+}^{0}¿$, is less than unity, salt accumulates near the positive electrode where lithium ions enter the electrolyte and is depleted at the negative electrode where lithium ions exit the electrolyte to react with (or intercalate into) the positive electrode. The result is a salt concentration gradient along the direction perpendicular to the current collectors while the total moles of salt within the entire electrolyte is conserved. This process is well understood in the case of homogeneous electrolytes.[6,7] During battery operation, we thus obtain regions of the electrolyte where the salt concentration is higher than the initial salt concentration and regions where it is lower. If the

volume of the electrolyte is fixed, the inescapable conclusion is that the solvent must rearrange to accommodate the salt concentration gradient.[8] For liquid electrolytes, solvent molecules can rearrange easily, and we expect a lower concentration of solvent in regions where there is a high salt concentration and a higher concentration of solvent in regions where there is a lower salt concentration.[9,10] It is not well understood how or if this occurs in polymer electrolytes where the rearrangement of the "solvent phase" is slow. In this work, we show that this process is complex for a block copolymer electrolyte and the local lamellar orientation relative to the electrodes plays an important role. Our results indicate that the process of block copolymer rearrangement limits the maximum current that can be sustained by a block copolymer electrolyte.

We employ small angle X-ray scattering (SAXS) to study the structure of a block copolymer electrolyte during dc polarization.[11–13] We focus on a system that has been well-characterized in the literature:[14–16] polystyrene-block-poly(ethylene oxide) (SEO) block copolymer doped with bis-(trifluoromethylsulfonyl)amine lithium salt (LiTFSI). Polystyrene (PS) provides mechanical rigidity to suppress lithium dendrite growth while poly(ethylene oxide) (PEO) solvates and conducts lithium ions. We previously reported similar experiments on an SEO/LiTFSI electrolyte with PS molecular weight, M_{PS}, of 1.7 kg mol^{-1} and PEO molecular weight, M_{PEO}, of 1.4 kg mol^{-1}, which exhibited phase transitions over the range of salt concentrations studied.[13] In this study, we used an SEO copolymer with M_{PS} = 19 kg mol^{-1} and M_{PEO} = 20 kg mol^{-1} which exhibits a lamellar morphology over all salt concentrations, measured as the molar ratio of LiTFSI to ethylene oxide moieties, $r=[LiTFSI]/[EO]$. Since the modulus of the electrolyte increases with molecular weight, a longer chain block copolymer is more practical for battery applications.[17] Our goal is to study the response of a practical nanostructured block

copolymer electrolyte subjected to dc polarization and understand the mechanisms which limit performance. The foundation of our understanding of ion transport through nanostructured electrolytes is based on numerous studies which examine structure-property relationships.[15,18–26] We extend this approach by considering the dynamic nature of these relationships when a dc current is applied.

The maximum current that can be sustained through an electrolyte, *i.e.*, the limiting current, $i_{\lim¿¿}$, depends on the salt concentration, r, and the distance between electrodes, L.[27,28] In this work, we study electrochemical cells comprising a block copolymer electrolyte sandwiched between two lithium electrodes (*i.e.*, lithium-lithium symmetric cells). We consider situations where a constant current is passed through the electrolyte. As concentration gradients develop, the potential drop across the electrolyte increases. Eventually, the potential drop will either stabilize at some constant value or diverge, depending on whether the applied current density is below or above the limiting current density. A stable potential is obtained if the diffusional flux of the anion down the salt concentration gradient matches the migratory flux due to the electric field; flow of ionic current for sustained periods thus requires the formation of a salt concentration gradient. The limiting current density typically coincides with the condition that the steady-state salt concentration at the negative electrode approaches zero. Above the limiting current, the potential begins to diverge because, in the absence of lithium ions at the electrode/electrolyte interface, electrons in the negative electrode begin to participate in irreversible parasitic reactions with the electrolyte.[29]

Experimental Methods

Materials. The polystyrene-*block*-poly(ethylene oxide) (SEO) block copolymer used in this study was synthesized, purified, and characterized using methods described by Teran et al.[30] and Hadjichristidis et al.[31] The block copolymer electrolyte (polystyrene (PS) molecular weight of 19 and poly(ethylene oxide) (PEO) molecular weight of 20 kg mol^{-1}) was prepared following the methods reported by Yuan et al.[32] to produce an SEO/LiTFSI mixture with $r = 0.16$. We use the notation SEO(xx-yy) to denote SEO block copolymers with molecular weight of the PS and PEO blocks equal to xx and yy kg mol^{-1}, respectively. Lithium metal with nominal thickness of 0.75 mm was purchased from MTI and scraped with a nylon brush to expose a fresh lithium surface. The lithium was then cut into a 3.18 mm diameter disk and pressed at 500 psi, resulting in a disk approximately 1 cm in diameter and 0.1 mm thick.

Electrochemical characterization of conductivity and limiting current. SEO samples for electrochemical measurements were prepared by placing electrolytes in annular spacers with inner diameters of 3.18 mm and hand-pressing them into pellets. Samples were hot-pressed at 90 ºC to create uniform, non-porous films. The polymer sample was sandwiched between stainless steel or lithium electrodes of known thickness. The total cell thickness was measured using a micrometer before attaching nickel current collectors and sealing the cell in polypropylene-lined aluminum pouch material. At this point, the cells were removed from the glovebox for testing. The inner diameter of the spacer and the thickness measurements allow for determination of the cell constants A and L, the electrochemically active area and distance between electrodes, respectively.

Ionic conductivity of samples with blocking electrodes (stainless steel), κ, was measured by ac impedance spectroscopy at 90 ºC. Prior to measurement, cells were annealed at 120 ºC for

at least 8 hours and then cooled to 90 °C. The bulk resistance, R_b, was determined by fitting an equivalent circuit and used to calculate the ionic conductivity, κ, via $\kappa = \dfrac{L}{R_b A}$.

The limiting current was measured by assembling cells with lithium electrodes and $L = 0.025$ cm. All measurements were performed at 90 °C. The cells were polarized at constant current until either a steady state potential was reached, or the potential diverged. After polarization, the current was set to zero and the potential relaxed until it stabilized around 0 V. For subsequent polarizations, the direction of the current was flipped.

SAXS measurements on samples with inert windows. SAXS characterization was performed on a series of electrolytes with different salt concentrations to obtain the domain spacing, d, as a function of r. We synthesized a series of electrolytes with salt concentrations ranging from $r = 0$ to 0.36. For each sample, electrolyte was hot pressed into an annular rubber spacer to create uniform, non-porous films with nominal thickness of 0.072 cm. Kapton windows with a thickness of 0.0025 cm were affixed on either side of the spacer and the sample was sealed in an air-free aluminum sample holder. The samples were then vacuum annealed at 120 °C for 8 h before bringing to the beamline for measurement. SAXS measurements were carried out at 90 °C on a custom-built heating stage. All SAXS experiments on samples with Kapton windows were performed at beamline 7.3.3. of the Advanced Light Source (ALS) at Lawrence Berkeley National Laboratory at an X-ray energy of 10 keV.[33] Silver behenate was used to determine the beam center and sample-to-detector distance. 2D scattering patterns were collected with a Pilatus3 2M detector (Dectris Ltd).

Preparation of electrochemical cells for simultaneous SAXS experiments. The polymer electrolytes were dried at 120 °C under active evacuation in a glovebox antechamber for 24 h

prior to constructing the cells for the simultaneous SAXS and electrochemical experiments. Lithium electrodes were pressed onto stainless steel current collectors and placed in the cell assembly which was machined out of poly(ether ether ketone) (PEEK). Polymer electrolyte was then hot pressed between the electrodes. Set screws were used to press the stainless-steel blocks closer together, until the distance between the two lithium electrodes was approximately 1.4 mm. (The distance between electrodes, L, was measured accurately at the beamline by X-ray transmission measurements, as detailed in Fig. S4 of the Supporting Information.) Excess polymer was then scraped away, and nickel tabs were affixed to the stainless-steel blocks. A reference channel, isolated from the electrochemical channel, was also filled with electrolyte of the same salt concentration. The reference channel was designed so that the path length traveled through the electrolyte by the X-ray beam was identical to the electrochemical channel. The PEEK assembly was then closed and sealed in aluminum-laminated pouch material with nickel tabs protruding. A picture of the cell assembly and dimensions is provided in Fig. S1 of the Supporting Information. After assembling the lithium-lithium symmetric cells, the samples were vacuum annealed for 120 °C for at least 8 h. The samples were then cooled to room temperature and brought to the beamline for testing. The samples were affixed to a heating stage custom-built for simultaneous SAXS and electrochemical measurements. The samples were allowed to thermally equilibrate for 1 h at 90 °C prior to polarization and then maintained at this temperature for the duration of the experiment.

Simultaneous SAXS and dc polarization experiments. All simultaneous SAXS and dc polarization experiments were performed at Stanford Synchrotron Radiation Light Source (SSRL) beamline 1−5 at SLAC National Accelerator Laboratory. A custom-built sample heating

stage was used for the measurements which allowed for up to three electrochemical cells to be studied simultaneously. The beam size was fixed at 700 μm (y-axis) by 200 μm (x-axis) by slits that were positioned downstream of a multilayer monochromator and toroidal focusing mirror, where the x-axis is parallel to the current direction (see Fig. 3a). While the beam is rectangular in shape at the sample, it is focused to a point at the detector plane. Our primary interest is on the scattered peak position and intensity, which is not impacted by the beam shape. The dimensions of the lithium electrodes were 0.195 x 0.395 cm. Thus, the electrolyte formed a rectangular prism where the 0.395 cm x L face was oriented with its normal parallel to the X-ray beam and the X-ray beam passed through 0.195 cm of electrolyte. Based on the direction of current flow, we expect the sample to be uniform in lamella structure along the y- and z-coordinates. The X-ray energy was 12 keV and the exposure time at each position was 10 s. The x- and y-coordinates of the cell were mapped out by scanning the beam across the sample and measuring the beam-stop diode intensity. The intensity reading from the diode was zero when the beam was positioned on the stainless-steel current collector and non-zero when passing through the lithium metal, polymer electrolyte, or PEEK. Intensity readings were used to calculate L (see Fig. S4 of the Supporting Information). Silver behenate was used to determine the beam center and sample-to-detector distance. 2D scattering patterns were captured on a SX165 CCD detector (Rayonix, LLC). The 2D scattering profiles were reduced to 1D profiles using the PyFAI package for Python.[34] We performed SAXS on the reference sample simultaneously with the electrochemical samples to check for changes in the beamline conditions that could result in variations in the data. We visually inspected the cells after the experiment and found no discoloration or visible changes to the cell, indicating beam damage was not an issue.

Electrochemical measurements. All electrochemical measurements were made using a Biologic VMP3 potentiostat. Ac impedance measurements were made in a frequency range from 1 MHz to 100 mHz with an amplitude of 80 mV.

Results and Discussion

Electrolyte properties as a function of salt concentration.

To understand the transient phase behavior of a block copolymer electrolyte in the presence of a salt concentration gradient between two lithium electrodes, we start by characterizing the electrolyte under quiescent conditions over the range of salt concentrations that may be encountered during polarization. LiTFSI selectively partitions into the PEO domains[35–37] and this affects the thermodynamic properties of the system.[21] One consequence is that the domain spacing increases as salt is added. The domain spacing, d, is defined as the distance between the center of two lamella of the same component. Using sample holders with inert Kapton windows, we performed SAXS on a series of SEO(19-20)/LiTFSI electrolytes to extract the d as a function of salt concentration, r. The domain spacing is related to the position of the first order scattering peak, $q^{\dot{\iota}}$, by Eqn. 1:

$$d=\frac{2\pi}{q^{\dot{\iota}}}.$$

(1)

The results are presented in Fig. 1a. The neat block copolymer (r = 0) has a domain spacing of 28.1 nm. The domain spacing increases rapidly with increasing salt concentration until r = 0.04 where d = 35.9 nm. Above r = 0.06, d increases more gradually and shows an approximately linear trend with r up until the highest salt concentration measured, r = 0.36, where d = 52.2 nm. Based on the data in Fig. 1a for individual electrolytes cast at different salt concentrations, we

have a straightforward approach to predict the spatial dependence of the domain spacing when a known salt concentration gradient forms across a lithium symmetric cell. This analysis, which relies on a quantitative relationship between d and r, is enabled by empirically fitting the data. The least squares fit using a sum of two exponential functions is given by the curve in Fig. 1a and the resulting expression is:

$$d\,(nm) = 149 - 114\exp[-0.421\,r] - 7.09\exp[-46.3\,r]. \tag{2}$$

Newman's concentrated solution theory allows us to predict the salt concentration and potential gradient across a lithium symmetric cell during polarization.[7] The steady-state concentration profile, r ¿), and potential drop, U_{ss}, can be determined using integral relationships when the conductivity, κ, current fraction, $\rho_{+¿¿}$, and a term related to the thermodynamics of the

electrolyte, $\dfrac{dU}{d\ln m}$, are known as a function of salt concentration, where U is the open circuit potential of a concentration cell and m is the salt molality. The details for modeling salt concentration profiles are discussed in refs [27,38,39]. Briefly, the salt concentration gradient at steady state, $r(x/L)$, can be determined from Eqn. 3 by an iterative process: 1) guess a salt concentration at $x/L = 0$, 2) calculate $r(x/L)$ based on the initial guess from Eqn. 6, 3) integrate $r(x/L)$ from 0 to 1 to determine the average salt concentration, and 4) iterate the initial guess until the calculated average salt concentration matches the desired value (in our case, $r = 0.16$). Equation 3 is given by:

$$\int_{r(x/L=0)}^{r(x/L=1)} J_1(r)\,dr = \frac{-iL}{F}\left(\frac{x}{L}\right), \tag{3}$$

where F is Faraday's constant and

12

$$J_1(r) = \kappa \left(\frac{dU}{d\ln m} \right) ¿ ¿$$
$$¿$$

Here, $z_{+¿¿}$ is the charge number of the cation, $v_{+¿¿}$ is the number of cations the salt dissociates

into, and ϕ_c is the volume fraction of the conducting phase. Once $r¿$) is known, the steady state

potential drop, U_{ss}, across the electrolyte can then be calculated by solving:

$$U_{ss}(x) = F \, z_{-¿} \, v_{\substack{-¿ \int\limits_{r(x¿¿=1)}^{r(x¿¿=0)} J_2|r|dr, ¿}} \quad (5)$$
$$¿$$

where $z_{-¿¿}$ is the charge number of the anion and $v_{-¿¿}$ is the number of anions the salt dissociates

into and

$$J_2(r) = \left(\frac{dU}{d\ln m} \right) ¿ ¿$$
$$¿$$

Derivations for Eqn. 6-9 are provided in ref [38]. The equations presented here are rearranged by

substituting expressions for the anion transference number with respect for the solvent velocity,

$t_{-¿^0¿}$, which is given by:

$$t_{-¿^0} = 1 - t_{+¿^0 = -¿¿} ¿$$
$$¿$$

where c is the salt concentration in moles per liter and D is the salt diffusion coefficient in cm^2 s$^-$

^{1}.

    In previous work, we demonstrated that $\rho_{+¿¿}$ and $\dfrac{dU}{d\ln m}$ in SEO/LiTFSI electrolytes

follow universal trends regardless of chain length and conducting phase volume fraction, given

by Eqn. 8 and 9:[21]

$$\rho_{+}=0.18-1.7r+6.3r^2, \quad (8)$$

$$\frac{dU}{d\ln m}(mV)=-74-66\ln m-13.8(\ln m)^2.$$
$$(9)$$

The dependence of ϕ_c on r is given by:

$$\phi_c=\frac{v_c}{v_c+\dfrac{M_{PS}M_{EO}}{M_S M_{PEO}}v_S},$$
$$(10)$$

where M_{PS} and M_{PEO} are the molecular weight of the PS and PEO blocks (19,000 and 20,000 g mol^{-1}, respectively), M_s and M_{EO} are the molar mass of the styrene and ethylene oxide monomers (104.2 and 44.05 g mol^{-1}, respectively), and v_c is the molar volume of the conducting phase (PEO

+ LiTFSI), given by $v_c=\dfrac{M_{EO}}{\rho_c(r)}$. The density of the conducting phase, $\rho_c(r)$, was taken from ref 40.

The implication of Eqns. 3-9 is that, for any SEO/LiTFSI electrolyte, we need only measure the ionic conductivity, κ, as a function of r to predict r) at steady state and U_{ss} for a given current density. We present κ as a function of r for SEO(19-20)/LiTFSI in Fig. 1b based on ac impedance spectroscopy preformed on cells with blocking (*i.e.*, stainless steel) electrodes. The data presented in Fig. 1b was obtained at 90 °C after annealing at 120 °C for 8 h. The conductivity of block copolymer electrolytes is a function of the lamella grain size which can change depending on the thermal history of the sample. We therefore kept the thermal history identical for all samples (see Experimental Section). The conductivity of SEO(19-20) increases

with salt concentration from the dilute limit until $r = 0.10$ and then plateaus at higher salt concentrations. The results are consistent with measurements on other block copolymer electrolytes which have been reported on in the literature, and we defer discussion of the relationship between κ and r to those references.[14,21,32,41,42] We fit the conductivity following the functional form presented in ref [43] and obtain:

$$\kappa \left(S\,c\,m^{-1} \right) = 0.00237\,r\,\exp\left[\frac{-r}{0.170} \right]$$

$$(11)$$

We can thus calculate $J_1(r)$ and $J_2(r)$ for SEO(19-20)/LiTFSI electrolytes using Eqn. 8-11 and the results are presented in Fig. S2 of the Supporting Information.
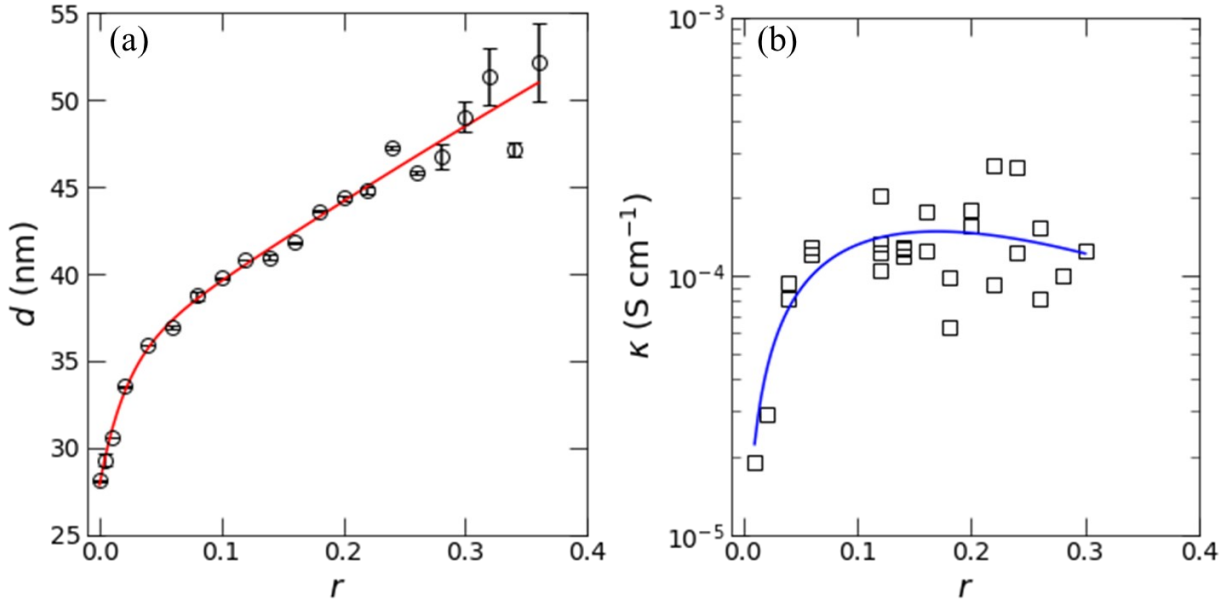
Figure 1. (a) Domain spacing, d, versus molar salt concentration, r, for a series of SEO(19-20)/ LiTFSI electrolytes at 90°C. The electrolyte exhibits a lamellar morphology at all salt concentrations. The red line is a double exponential fit to the data given by Equation 2. (b) Ionic conductivity, κ, versus r measured from ac impedance spectroscopy in cells with blocking electrodes at 90°C. Each data point represents a measurement from a unique cell. The black

We are now poised to predict salt concentration profiles at steady state and U_{ss} for various current densities. We test these predictions by experimentally measuring the voltage versus time behavior (at constant polarization current) of our electrolyte with initially uniform salt concentration of $r = 0.16$ in the long-time limit. Lithium-lithium symmetric cells were constructed with $L = 0.025$ cm. The cells were polarized at constant current density, i, and the potential was measured. If iL is below $i_{\lim}L$, it is expected that the potential will plateau and reach a steady-state value, U_{ss}, indicating that a time-independent concentration profile is achieved. The timescale on which the cell reaches steady state is proportional to L^2. (For the simultaneous polarization and SAXS experiments, which we discuss in the next section, $L \sim 0.15$ cm and the timescales are expected to be about 36 times longer relative to the cells with $L = 0.025$ cm.) If iL is above $i_{\lim}L$, then the potential will diverge instead of reaching a plateau. In Fig. 2a, we plot the potential response for a series of applied current densities: $iL = 0.025$ (red trace), 0.10 (orange trace), 0.40 (yellow trace), 0.60 (green trace), 1.6 (blue trace), 3.2 (purple trace), and 6.4 μA cm^{-1} (black trace). The cell potential, U, is the potential drop across the electrolyte. Experimentally, we measure the potential drop across the current collectors, ΔV, which includes a significant contribution from the resistance at the lithium electrode/electrolyte interfaces. We calculate the interfacial potential drop, $\Delta V_{\int}$, by multiplying the interfacial resistance measured from ac impedance spectroscopy and the current $(\Delta V_{\int i = R_{\int iA} i}$.[44] The interfacial resistance was approximately constant throughout each polarization experiment, so $\Delta V_{\int}$ is assumed to be independent of time (see Fig. S5 in the Supporting Information). The data in Fig. 2a and b have been corrected by subtracting $\Delta V_{\int}$ from the measured voltage (

$U = \Delta V - \Delta V_{\int \dot{c}\dot{c}}$). In Fig. 2b, we plot U_{ss} versus iL with red star makers. We see excellent agreement between theory and experiment up to iL = 3.2 μA cm^{-1}. At $iL = \dot{c}$ 6.4 μA cm^{-1}, the potential diverges after about 5 h in Fig. 2a. In Fig. 2b, we denote this experimental observation by the red dashed line which extends towards infinity above iL = 3.2 μA cm^{-1}. We estimate $i_{\lim \dot{c}\dot{c}}$ as the average between the largest sustained current density and the lowest value measured which resulted in a divergence of the potential. Thus, the limiting current measured experimentally is estimated to be 4.8 ± 1.6 μA cm^{-1}.

Using Eqns. 3-11, we can predict $i_{\lim \dot{c}\dot{c}}$ by extrapolating to the case where the salt concentration reaches zero at the plating electrode (see Fig. S3 in the Supporting Information).[27,38,39] In Fig. 2c, we plot theoretically predicted limiting current for SEO(19-20)/LiTFSI electrolytes with r ranging from 0.02 to 0.16 as open black circles. The limiting current normalized by the distance between electrodes, $i_{\lim \dot{c} L \dot{c}}$, is plotted versus r; we choose this format because results obtained using symmetric cells with other values of L can be compared directly with the data presented here. We note that these predictions are made using no adjustable parameters. We see the expected behavior that $i_{\lim \dot{c} L \dot{c}}$ increases monotonically with salt concentration from 2.12 μA cm^{-1} at r = 0.03 to 10.5 μA cm^{-1} at r = 0.16. The red star in Fig. 2c represents the experimentally measured limiting current. The experimental value is approximately a factor of two lower than that predicted by concentrated solution theory. One of the motivations for the simultaneous SAXS and polarization experiments described in the next section is to investigate the reason for this discrepancy.
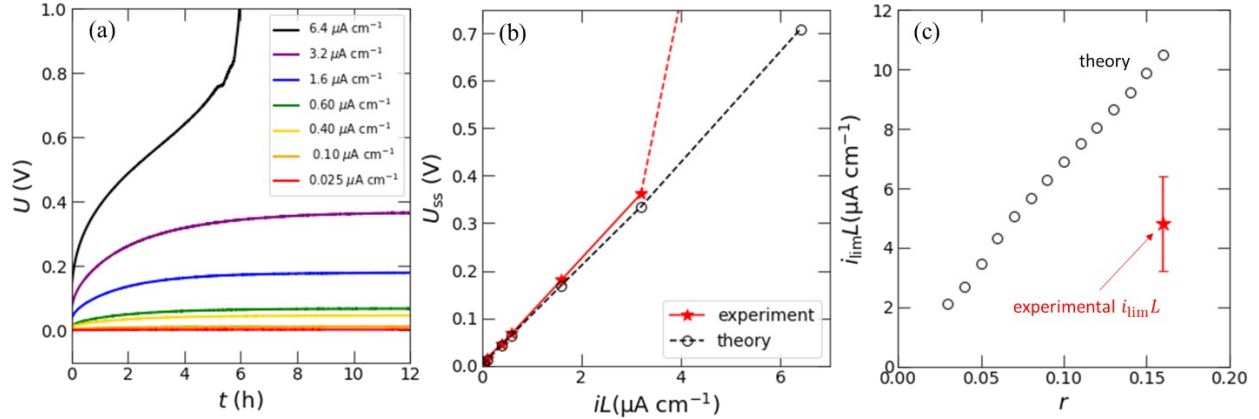
Figure 2. Comparison of an experimental limiting current measurement to theory. (a) Experimental measurement of the limiting current. The potential drop across the electrolyte, U, is plotted versus time, t, for increasing current densities from $iL = 0.025$ to 6.4 µA cm^{-1} with $L = 0.025$ cm. A steady-state potential, U_{ss} is obtained for all currents except $iL = 6.4$ µA cm^{-1} where U diverges after 5 h. We take the experimental limiting current to be the average of the lowest unsustainable current density (6.4 µA cm^{-1}) and the highest sustainable current density (3.2 µA cm^{-1}). The error bars in (c) depict the fact that the true value of $i_{\lim} L$ may lie anywhere between these two values. (b) U_{ss} versus iL from experiment (red stars) and theory (black open circles). The dashed red line indicates that the steady state potential diverges to infinity at $iL = 6.4$ µA cm^{-1}. (c) Normalized limiting current, $i_{\lim} L$, versus molar salt concentration, r. Black open circles represent the predicted $i_{\lim} L$ from concentrated solution theory. The data point marked by a red star indicates the value of $i_{\lim} L$ measured experimentally.

Gradients in domain spacing as a function of current density.

To monitor the structure of the SEO(19-20) with $r = 0.16$ electrolyte during polarization, we built a custom electrochemical cell to allow simultaneous SAXS measurements. This cell is shown schematically in Fig. 3a. The lithium electrodes are in the y-z plane such that the nominal direction of ionic current is parallel to the x-axis. In Fig. 3b, we show an example of a SAXS pattern obtained from SEO(19-20) where the incident beam is oriented in the z-direction. Our sample, which is made by pressing the freeze-dried electrolyte into the sample holder, consists of lamellar grains oriented in different directions. The information in a 2D SAXS pattern from a collection of lamellar grains results from lamellae which have normal vectors in the plane

18

perpendicular to the incident beam (the x-y plane, in our case); the normal vector is defined to be perpendicular to the nominal interfaces between adjacent lamellae.[45] By scanning the beam along the x-axis, the 2D scattering patterns contain information about the structure of lamellae with normal vectors in the x-y plane along the axis which the salt concentration gradient forms in a dc polarization experiment. We define the azimuthal angle, χ, in Fig. 3b and denote $\chi = 0°$ along the y-axis, pointing upwards and increasing counterclockwise. The SAXS pattern is divided into 16 sectors as shown in Fig. 3b and the cartoons in each sector indicate the orientation of lamellar grains which give rise to scattering in that sector. By analyzing data at $\chi = 0$ and $180°$ (as defined in Fig. 3b) we obtain information about grains with PS-PEO interfaces oriented parallel to the flow of ionic current (we call these lamellae $LAM_{¿∨¿¿}$, and note that their normal vectors are parallel to the y-axis). For $\chi = 90$ and $270°$, we obtain information about grains with PS-PEO interfaces oriented perpendicular to the flow of ionic current (we call these lamellae LAM , and note that their normal vectors are perpendicular to the y-axis).
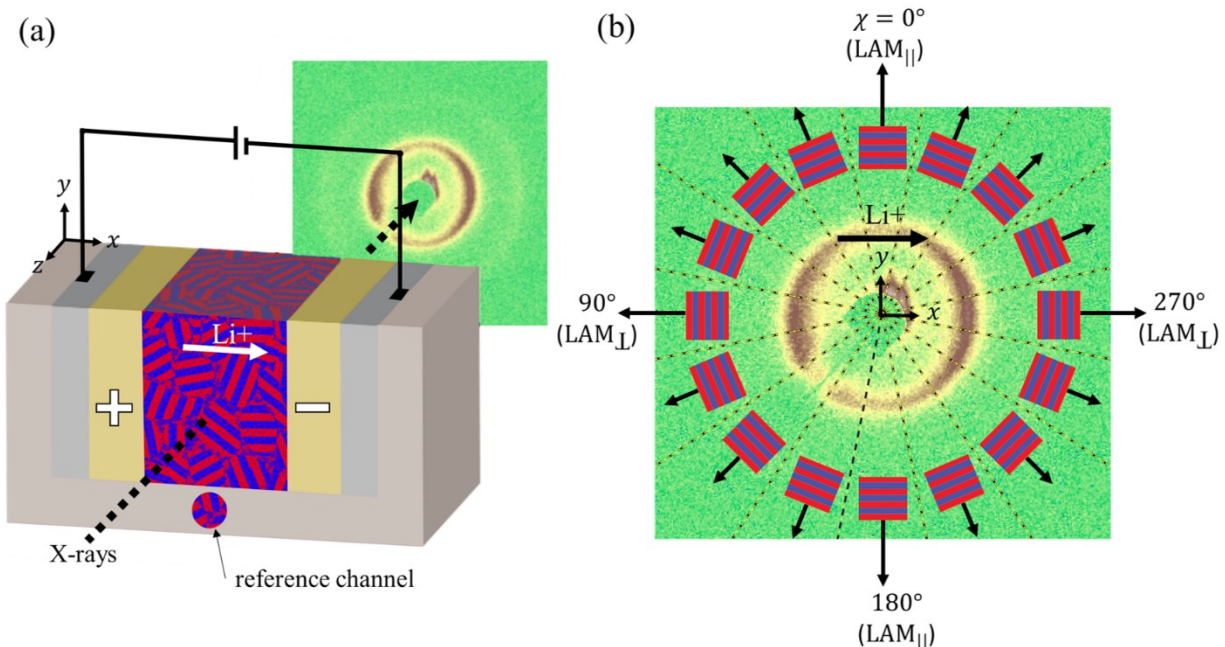
Figure 3. (a) Schematic representation of the simultaneous polarization and SAXS experiment. An SEO/LiTFSI electrolyte with randomly oriented grains is sandwiched between two lithium electrodes with current passing parallel to the x-axis. X-rays pass parallel to the z-axis, perpendicular to the current. Scanning the beam along the x-axis allows for spatial resolution between the electrodes. A reference channel filled with electrolyte was placed next to the electrochemical cell. (b) Characteristic 2D SAXS pattern obtained from experiments. The pattern is divided into 16 sectors defined by the azimuthal angle, χ. Scattering data in each sector corresponds to lamellae oriented with the angle between the vector normal to the PEO-PS interfaces and the positive y-axis equal to χ. The cartoons in each sector show the lamellar orientation with their respective normal vectors.

Using the experimental geometry shown schematically in Fig. 3, we studied three lithium-lithium symmetric cells comprising an SEO(19-20)/LiTFSI electrolyte with $r = 0.16$ at three current densities. The beam was aligned so that the 200 μm beam dimension was along the x-axis of the cell (i.e., the axis perpendicular to the planar electrodes, which is the direction of ionic current flow). The 700 μm dimension was along the y-axis of the cell and in the center of the channel along the y-axis. The sample was scanned in 100 μm increments along the x-axis, beginning and ending over the stainless-steel current collectors. When the beam was aligned over the stainless-steel, the beam was completely attenuated, and the transmitted and scattered

intensity were both zero. We used the transmitted intensity to define the coordinates and measure L for each cell (see Fig. S4 in the Supporting Information). We define the initial time, $t = 0$, as the first moment of polarization. Throughout this work, we discuss the current in terms of iL which is the current, I (µA), divided by the electrode surface area, $A = 0.077$ cm^2, for all three cells, multiplied by the distance between electrodes, L (cm).

We begin by analyzing SAXS data for cells polarized at $iL = 0.926$ µA cm^{-1} (Fig. 4a), 1.96 µA cm^{-1} (Fig. 4b), and 3.74 µA cm^{-1} (Fig. 4c). An example of a 2D SAXS pattern obtained from these experiments is presented in Figure 3b. A 360° azimuthal average of the data was performed to obtain 1D SAXS profiles of the scattered intensity, I, as a function of the scattering vector, q. We obtain the domain spacing by fitting the primary scattering peak to a pseudo-Voight function as described in the Supporting Information to obtain $q^{\dot\iota}$ and calculating d from Eqn. 1. In Fig. 4, we plot d as a function of normalized position between the electrodes, x/L. Lithium stripping occurs at the positive electrode where $x/L = 0$ and lithium plating occurs at the negative electrode where $x/L = 1$. The top panel in each figure (Fig. 4a-c) shows the potential response, U, of the cell as a function of time. The black dashed line represents U_{ss} predicted from theory. In all cases, the measured potential stays below the predicted value and does not reach a clear plateau before the experiment was halted at $t = 48$ h, mainly due to limited access to the SAXS instrument. The rainbow color scheme in the top panel and main figure are coordinated such that the color of the data points on the U vs t plot correspond to the time which the data set of the d versus x/L was obtained. Purple data sets were obtained near the beginning of the polarization step ($t = 0$ h) and red data sets were obtained near the end ($t = 47$ h).

In Fig. 4a, a constant current density of 6.34 µA cm^{-2} was applied across a cell with L = 0.140 cm (iL = 0.926 µA cm^{-1}). At t = 0 h, the average domain spacing across all positions is 42.4 nm. The domain spacing is not completely uniform initially; d = 42.3 nm near the center of the cell and d = 42.6 nm near the electrodes. We suspect this difference (less than 1% of the domain spacing) is due to uneven stress distribution on the lamella during sample preparation. This trend is also seen in Fig. 4b and 4c. In Fig. 4b, a current density of 13.5 µA cm^{-2} was applied across a cell with L = 0.145 cm (iL = 1.96 µA cm^{-1}), and in Fig. 4c, a current density of 27.3 µA cm^{-2} was applied across a cell with L = 0.137 cm (iL = 3.74 µA cm^{-1}). For each cell, d increases near the positive electrode where local salt concentration increases and decreases near the negative electrode where local salt concentration decreases. The gradient in d develops near the electrodes first, then propagates towards the center of the cell and becomes more linear with time. To highlight this, we drew lines through the d versus x/L data sets corresponding to t = 4.7 and 19.6 h along with the first (t = 0 h) and last data (t = 46.6 h) set. The qualitative observation that the domain spacing changes first near the electrodes before propagating into the center of the cell is consistent with predictions of time-dependent concentration profiles from concentrated solution theory.[46]

As the current increases from Fig. 4a to 4c, the magnitude of the domain spacing gradient increases. For the lowest current density, the difference in d between the positive and negative electrodes at t = 46.6 h is 1.63 nm, for the middle current density, it is 3.84 nm, and for the highest current density, it is 9.08 nm. A larger salt concentration gradient is expected for higher current densities as the flux of the anion due to migration is larger and thus a larger diffusive flux is required to match it and achieve steady state. Interestingly, the domain spacing gradients are

not symmetric; the increase in domain spacing at the positive electrode is larger than the magnitude of the decrease in domain spacing at the negative electrode. This effect is most prominent for the largest current density in Fig. 4c. For all three current densities, the point where d shifts from increasing to decreasing is at a position $x/L \approx 0.6$. We next turn to Eqn. 2 to convert the measured domain spacings into local salt concentrations as they can be directly compared with theoretical predictions.
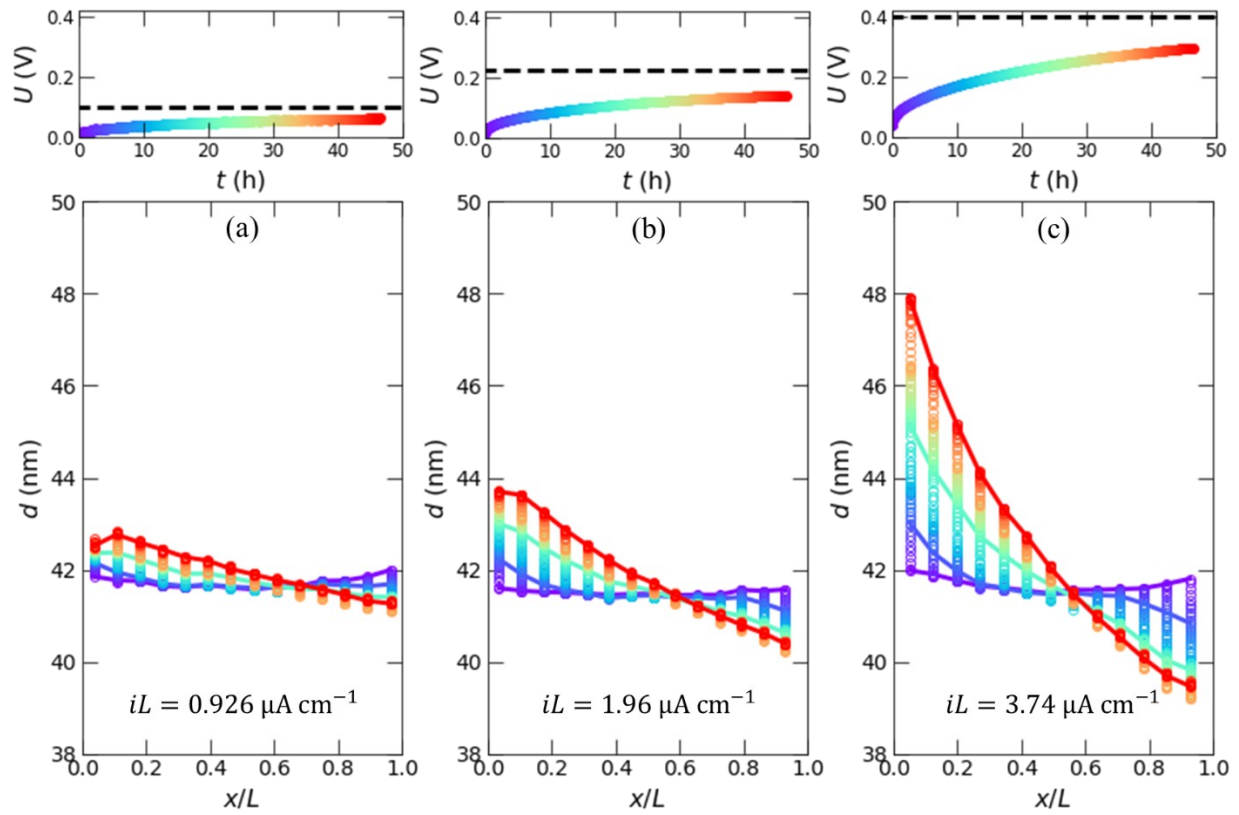

Figure 4. Results from simultaneous polarization and SAXS experiments at three current densities. The potential drop across the electrolyte, U, versus time, t, is plotted in the top panel of each figure. The dashed line represents the steady state potential (U_{ss}) predicted from concentrated solution theory. In the main panel, the domain spacing, d, is plotted versus normalized cell position, x/L, for the cell polarized at (1) $iL = 0.962$ μA cm^{-1}, (b) 1.96 μA cm^{-1}, and (c) 3.74 μA cm^{-1}. The color of each data set corresponds with the U versus t plot in the top panel. Purple data sets were obtained at the beginning of polarization ($t = 0$ h) and red data sets were obtained at the end of polarization ($t = 46.6$ h).

Domain spacing as a proxy for salt concentration.

For each data point in Fig. 4a-c, we calculate a local salt concentration from Eqn. 2 to obtain $r(x/L,t)$ for each cell, and the results are plotted as data points in Fig. 5, following the same color scheme as Fig. 4. The black dashed lines represent the nominal initial salt concentration ($r = 0.16$) of the cell, and the solid black lines represent the steady state salt concentration gradient predicted from theory. Based on Fig. 2a, we calculate the ratio of the current density to the limiting current, $i/i_{\lim}¿¿$. Because the predicted limiting current differs significantly from the measured limiting current, we report the ratio of the applied current to both the experimental and theoretical limiting currents, $i_{\lim,expt}$ and $i_{\lim,theory}$. The applied current density is 20%, 44%, and 80% of $i_{\lim,expt}$ and 9.0%, 20%, and 36% of $i_{\lim,theory}$ for Fig. 5a, b, and c, respectively. In Fig. 5a and b, we see good agreement between the experiment and the theory; the magnitude of the salt concentration near the end of the polarization experiment matches the predicted salt concentration gradient. Conversely, the agreement with $r(x/L)$ is poor in Fig. 5c at $iL = 3.74$ µA cm^{-1}.
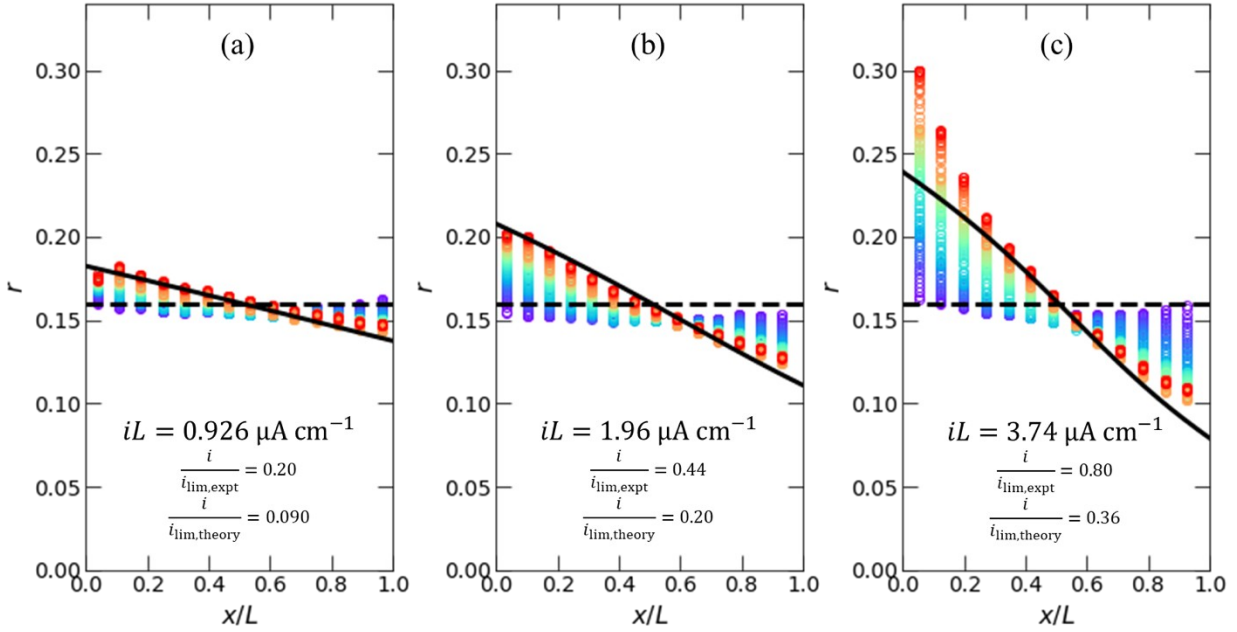
Figure 5. Molar salt concentration, r, versus normalized cell position, x/L based on converting the domain spacing, d, presented in Fig. 4 to r with Eqn. 2. We report the ratio of the applied current to the experimental limiting current, $i_{\lim,expt}$ and the theoretical limiting current, $i_{\lim,theory}$. (a) Data obtained with iL = 0.926 μA cm^{-1}. (b) Data obtained with iL = 1.96 μA cm^{-1}. (c) Data obtained with iL = 3.74 μA cm^{-1}. The color scheme for each data set matches that presented in Fig. 4a-c. The dashed black line represents the nominal initial salt concentration, r= 0.16. The solid black line represents the predicted steady-state salt concentration gradient from theory.

In Fig. 5c, using the domain spacing as a proxy for salt concentration results in local values of r which are significantly greater than the theory across the entire cell. The experimental salt concentration averaged across all positions calculated from Eqn. 2 in Fig. 5c is $r = 0.157$ at t = 0 h and $r = 0.186$ at $t = 46.6$ h, an increase of 18%. Because the average salt concentration must be conserved throughout the experiment, we conclude that the assumed relationship between r and d, which was based on measurements on samples at equilibrium, is strictly valid when the magnitude of the ionic current that flows through the sample is well below the limiting current. Nevertheless, we obtain considerable insight into the origin of the observed gradients in d under applied electric fields by combining equilibrium measurements of domain spacing with

concentrated solution theory. Agreement between theory and experiment is reasonable for $i/i_{\lim,expt} < 0.5$ where we see good agreement between theoretical and experimental U_{ss} versus iL data in Fig. 2b.

Swelling and contracting lamellae at high current density.

To gain deeper insight into the swelling and contraction of the lamellae at high current density, we performed the following experiments. After polarizing the cell in Fig. 4a at 0.926 µA cm^{-1} for 46.6 h, we increased the current by a factor of 12 to 11.1 µA cm^{-1} (*i.e.*, $i/i_{\lim,expt}$ = 2.4 and $i/i_{\lim,theory}$ = 1.07). The potential of the cell is plotted as a function of time in Fig. 6a beginning at t = 46.6 h when the current was abruptly increased in a blue to green color scheme. At that time, the potential jumps from 0.08 V to 0.2 V and then steadily increases. At t = 58 h, there is an inflection point and the potential diverges. A cutoff voltage was set at 1.0 V, and the cell was switched to open circuit (i = 0 µA cm^{-2}) at t = 61.1 h. The potential then begins to decay, plotted in a blue to pink color scheme, as the concentration gradient relaxes.

Throughout the experiment, we measured $d(x)$ as a function of time. We define the change in domain spacing, Δd, by Eqn. 12:

$$\Delta d(x/L,t)=d(x/L,t)-d(x/L,t=0) \tag{12}$$

Recall that $t=0$ is at the beginning of the first polarization step at 0.926 µA cm^{-1}, so the quantity $\Delta d(x/L,t)$ reflects the change in domain spacing from the quiescent, r = 0.16 electrolyte. In Fig. 6b, we plot Δd as a function of normalized position in the cell from t = 0 to 61.1 h. Data sets plotted with black markers represent Δd during the initial polarization at 0.926 µA cm^{-1}. The magnitude of Δd is less than 2 nm during this time (see Fig. 4a). Data for 46.6 < t (h) < 61.1 is

plotted in a blue-to-green color scheme where the color corresponds to the U versus t data in Fig. 6a. The right axis of Fig. 6b represents the percent change of the domain spacing from the nominal initial value of 42.4 nm (averaged over all x/L at t = 0 h). At x/L = 0.088 (near the lithium stripping electrode), Δd reaches 10.8 nm at t = 61.1 h, an increase of 25.4 % from the quiescent state. At x/L = 0.93 (near the lithium plating electrode), we measure Δd of -4.4 nm at t = 61.1 h, a decrease of 10.4 % from the quiescent state. This difference between Δd at x/L = 0.088 and 0.93 highlights the point that the swelling of the salt rich lamellae is not compensated by the contracting of the salt deficient lamellae. We take this analysis a step further by fitting the data set at t = 61.1 h to a 5th order polynomial plotted as a red in line in Fig. 6b and given by:

$$\Delta d = -272(x/L)^5 + 816(x/L)^4 - 955(x/L)^3 + 542(x/L)^2 - 158(x/L) + 21.0 \qquad (13)$$

Because the cell is operating above the limiting current, the shape of d vs x/L when the potential diverges (green data set) is non-linear: the gradient in d is most severe near the electrodes. The area under the curve (calculated by integrating Eqn. 13 from x/L = 0 to 1) is an average of 1.6 nm. This implies that the average increase in d is 1.6 nm, or 3.8% from the quiescent state. Based on these significant changes in the domain spacing, it is instructive to analyze the scattering profiles more closely.

In Fig. 6c and d, we present the 1D SAXS profiles during polarization (t = 46 to 61 h) for the x/L = 0.088 (highlighted by the dashed gold box in Fig. 6b) and x/L = 0.93 (highlighted by the dashed purple box in Fig. 6b) positions, respectively. We plot the scattered intensity from the sample $I_s(q)$ divided by a constant reference intensity, I_{ref}. I_{ref} is the maximum intensity of the primary scattering peak of the reference sample (as described in the Experimental section). The scattering from the reference sample was measured once for each data set in Fig. 6b. We use the

same color scheme in Fig. 6c and 6d to denote the time of each data set. Our main interest is to investigate if there are any signatures of the lamellar structure being disrupted near the electrodes during the extreme polarization conditions. Overall, we see a shift of the primary scattering peak to lower q (higher domain spacing) in Fig. 6c, but the character of the peak remains consistent throughout the experiment. We do not observe the emergence of new peaks, indicating that the lamellar structure is preserved at all times and locations. The gradual changes in peak intensity are attributed to the change in scattering contrast between the lamella associated with changing salt concentration in the PEO-rich domains. The same is true in Fig. 6d as the peak shifts to higher q (lower domain spacing). In Fig. 6e and 6f, we show the 1D SAXS patterns obtained during the open circuit relaxation step (t = 61 to 80 h) at x/L = 0.088 and 0.93, respectively. Again, the character of the primary scattering peak is maintained as the peak position shifts towards the initial peak position prior to polarization.
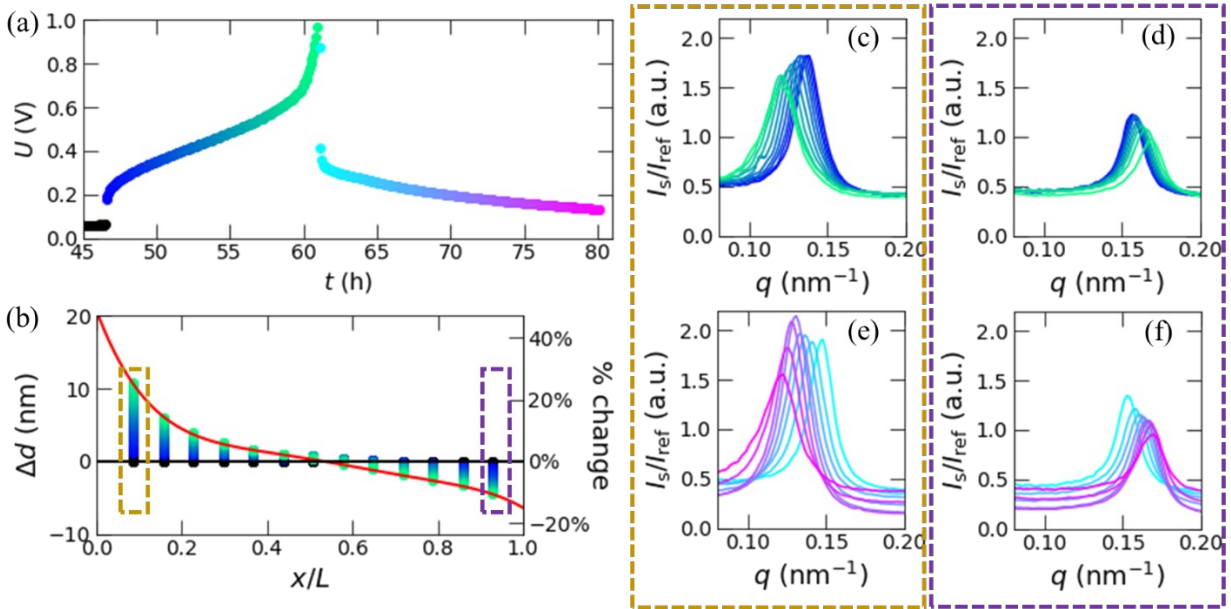
Figure 6. Results from simultaneous polarization and SAXS experiments performed at a current density above the limiting current, iL = 11.1 μA cm^{-1}. The current was increased from 0.926 μA

cm^{-1} at t = 46.6 h (data for t < 46.6 h is presented in Figs. 4a and 5a at the lower current density). (a) Potential drop across the electrolyte, U, versus t. For 46.6 < t (h) < 61.1, a constant current of iL = 11.1 µA cm^{-1} was applied and U is plotted in a blue to green color scheme. At t = 61.1 h, the cell was switched to open circuit (iL = 0) and the open circuit cell potential is plotted in a blue to pink color scheme. (b) Change in domain spacing, Δd, defined by Eqn. 7 versus t for the constant current polarization for 46.6 < t (h) < 61.1. Data sets plotted with black symbols were obtained during the 0.926 µA cm^{-1} polarization for t < 46.6 h. The blue to green color scheme of the remaining data set corresponds with the U versus t plot in (a). The red trace is a polynomial fit to the final data set at t = 61.1 h (green data points). 360° azimuthal averages of selected 2D SAXS patterns are presented in (c) through (e) with colors corresponding to the U versus t data in (a). (c) $I(q)$ plots for 46.6 < t (h) < 61.1 during the 11.1 µA cm^{-1} polarization at x/L = 0.088 and (d) x/L = 0.93. (e) $I(q)$ plots for t > 61.1 h when the cell is at open circuit measured at x/L = 0.088 and (f) x/L = 0.93. The gold and purple dashed boxes in (b) through (f) highlight data obtained at x/L = 0.088 and 0.93, respectively.

Lamellar orientation order parameter.

  To further investigate the extent to which the lamella may rearrange due to polarization, we calculated an orientation parameter for the electrolyte as a function of position and time. For each scan, the scattering pattern was divided into 36 sectors and averaged to obtain $I(q)$ for each sector. To compare the total scattered intensity for each grain orientation, $Q(\chi)$, we integrated $q^2 I(q)$ over the primary scattering peak for each sector. The orientation parameter, f, was calculated according to Eqn. 14:

$$f = \frac{3\langle \cos^2 \chi \rangle - 1}{2} \tag{14}$$

using Eqn. 15,

$$\langle \cos^2\chi \rangle = \frac{\displaystyle\int_0^{90} Q(\chi)\cos^2(\chi)\sin(\chi)\,d\chi}{\displaystyle\int_0^{90} Q(\chi)\sin(\chi)\,d\chi} \tag{15}$$

where $0°$ is defined such that it corresponds to lamellae with normal vectors perpendicular to the direction of current flow, as shown in Fig. 3b. Our analysis is based on the commonly used Herman's orientation parameter.[47–49] An orientation parameter $f = 1$ describes a lamellar sample where all grains are oriented with PS-PEO interfaces perpendicular to the direction of curent flow. For a sample with all PS-PEO interfaces oriented parallel to the direction of curent flow, $f = -0.5$. Randomly oriented lamellae correspond to $f = 0$.

The $Q(\chi)$ data ranges from $\chi = 0$ to $360°$, while in Eqn. 15 we restrict the analysis to only include data from $\chi = 0$ to $90°$ which is justified by symettry in the 2D SAXS patterns. A single lamellar grain generates identical scattering along two azimuths separated by $180°$. There is an additional plane of symmetry as grains oriented with $\chi = \pm\alpha$ for $0° < \alpha < 180°$ are identical from an electrochemical standpoint. To minimize noise in the data, we thus averaged the four quadrants of our data by first adding $Q(\chi)$ from 180 to $360°$ to the $Q(\chi)$ from 0 to $180°$. Next, we folded the resulting data, which ranges from 0 to $180°$, around $\chi = 90°$, thus resulting in $Q(\chi)$ that includes data from all four quadrants with χ ranging from 0 to $90°$. This data set of $Q(0 < \chi < 90°)$ was numerically integrated to obtain $\langle \cos^2\chi \rangle$ according to Eqn. 15.

The resulting orientation parameter, $f(t)$ is presented in Fig. 7 for each postion in the cell with iL 1.96 µA cm⁻¹. Similar plots for the other two cells can be found in Fig. S9 of the Supporting Information, and are qualitatively similar. At all positions, f is approximately -0.18 ± 0.03, with little change over time. This indicates that before any current is applied, the lamellar grains have a slight preference for orientations such that the PS-PEO interfaces are parallel to the direction of current flow. This orientation was likely introduced by the mechanical force necessary to deform the electrolyte and fill the cell. Electrochemcial polarization does not affect the distribution of grain orientations. If lamellar grains were to break up and re-form during electrochemical polarization, one would expect newly formed lamellae either to be randomly oriented, corresponding to $f = 0$, or to form with a new prefential orientation due to current flow. In either case, we would expect to observe f which varies with time. The observation that f is time-invariant suggests that the grain structure remains relatively constant throughout the experiment.
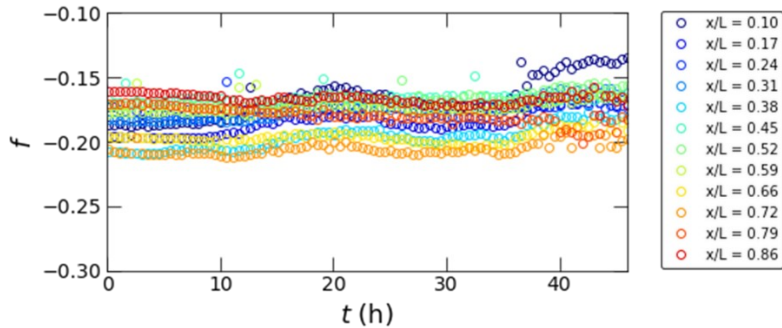
Figure 7. Orientation parameter, f, versus time, t, for the cell polarized at $iL = 1.96$ µA cm⁻¹ for positions ranging from $x/L = 0.10$ to 0.86. f is approximately constant with time across all positions, indicating that polarization does not induce grain alignment or dealignment.

Orientation dependence of lamellar distortion.

We next analyze how different orientations of lamella swell and contract in response to the salt concentration gradient. We focus our attention on the data sets obtained right before the cells are switched to open circuit. We divide the 2D scattering pattern into 16 sectors as shown in Fig. 3b to obtain $I(\chi)$ where χ represents the angle at the center of the sector. We follow the same peak fitting procedure as discussed previously to obtain $d(\chi)$ from the 2D scattering plots. Before polarization, we find that $d(\chi)$ was not constant. To account for this, we redefine the quantity Δd for a fixed position x/L in Eqn. 16:

$$\Delta d(\chi,t)=d(\chi,t)-d(\chi,t=0) \tag{16}$$

In Figure 8a-c, we plot Δd as a function of χ for each position in the cell for the cells polarized at (a) iL = 1.96 µA cm^{-1} (b) iL = 3.74 µA cm^{-1}, and (c) iL = 11.1 µA cm^{-1}. From top to bottom, x/L increases from 0.10 to 0.86. Near the positive electrode (*i.e.*, x/L < 0.4), Δd > 0 for all χ and there are local maxima at χ = 90° and 270°. Near the center of the cell, Δd is approximately equal zero for all values of χ. Near the negative electrode (i.e. x/L > 0.6), Δd < 0 for all χ and there are local minima at χ = 90° and 270°. The results presented in Fig. 8a-c show that grains with PS-PEO interfaces perpendicular to the flow of ionic current ($LAM_\perp$) undergo greater expansion (near the positive electrode) or contraction (near the negative electrode) when compared to those with PS-PEO interfaces oriented parallel to the flow of ionic current ($LAM_{\parallel}$). To highlight this point, we plot the difference in lamella spacing between $LAM_\perp$ and $LAM_{\parallel}$, $d_{LAM_\perp}-d_{LAM_{\parallel}}$, in Fig. 8d. The color of each data point in Fig. 8d corresponds to the data set of the same color in Fig. 8a-c. As the concentration gradient builds up, the $LAM_\perp$ near the positive electrode are swollen between 0.6 and 1.2 nm larger than $LAM_{\parallel}$. Near the negative electrode, the $LAM_\perp$ are between 0.2 and 1.2 nm smaller than the $LAM_{\parallel}$. Figures 7

and 8 indicate that the χ dependence of domain swelling and contracting is decoupled from any preferential grain orientation that was introduced during sample preparation.

The orientation-dependent distortion of lamellae shown in Fig. 8a-d indicates that the salt which is preferentially depleted from $LAM_\perp$ at the negative electrode preferentially accumulates in $LAM_\perp$ near the positive electrode. In a randomly oriented lamellar sample, one would conclude that grains in the $LAM_{\parallel \vee \perp \perp}$ orientation contribute the most to dc conductivity relative to any other orientation, while those in the $LAM_\perp$ do not contribute to the dc conductivity.[50] Our analysis shows that $LAM_\perp$ also play a critical, but more subtle, role in ion transport. The swelling and contracting of the lamellae are required to allow the formation of a salt concentration gradient and thus sustain the applied current, and a larger portion of this volume change is accommodated by those lamellae in the $LAM_\perp$ orientation. While a lamellar sample with only the $LAM_\perp$ orientation would not be desirable as there would be no path for ionic current to pass between the electrodes, one with only the $LAM_{\parallel \vee \perp \perp}$ orientation may also be undesirable because the resistance to volume change would reduce the limiting current. Therefore, we ~~may conclude~~ hypothesize that a collection of lamellar grains with a distribution of orientations is likely to lead to the largest limiting current due to the need to accommodate both large ionic currents and to accommodate large salt concentration gradients. Testing of this hypothesis would require control over the distribution of grain orientations prior to polarizing the cell.

We take our analysis a step further by using Eqn. 2 to estimate the local salt concentration in the lamellar grains as a function of χ. The results are shown on the right axis of Fig. 8d. Although we have discussed that the conversion from d to r fails quantitatively at high current densities, we do expect qualitatively that for two grains at the same x/L but with

different d, the grain with higher d will have higher local r. Thus, by calculating r versus χ for each position, we get an approximation of how the salt concentration varies in grains with different orientations. Based on Fig. 8d, r is about 0.03 higher in $LAM_\perp$ compared to $LAM_{\parallel}$ near the salt rich electrode, and about 0.03 lower near the salt deficient electrode for the cell polarized above the limiting current at $iL = 11.1$ µA cm⁻¹. These results suggest that salt concentration is non-uniform in along all three axes (x, y, and z), not just along the axis of ion transport (x). For the y- and z- axis, the concentration heterogeneity is on the length scale of the grain size (typically a few microns), while along the x-axis, the concentration gradient is on the length scale of L. In previous work, we identified the formation of concentration hotspots in SEO(1.7-1.4).[13] This new insight suggest that the nucleation of these hotspots likely emerges from grains in the $LAM_\perp$ orientation where salt accumulates more heavily.
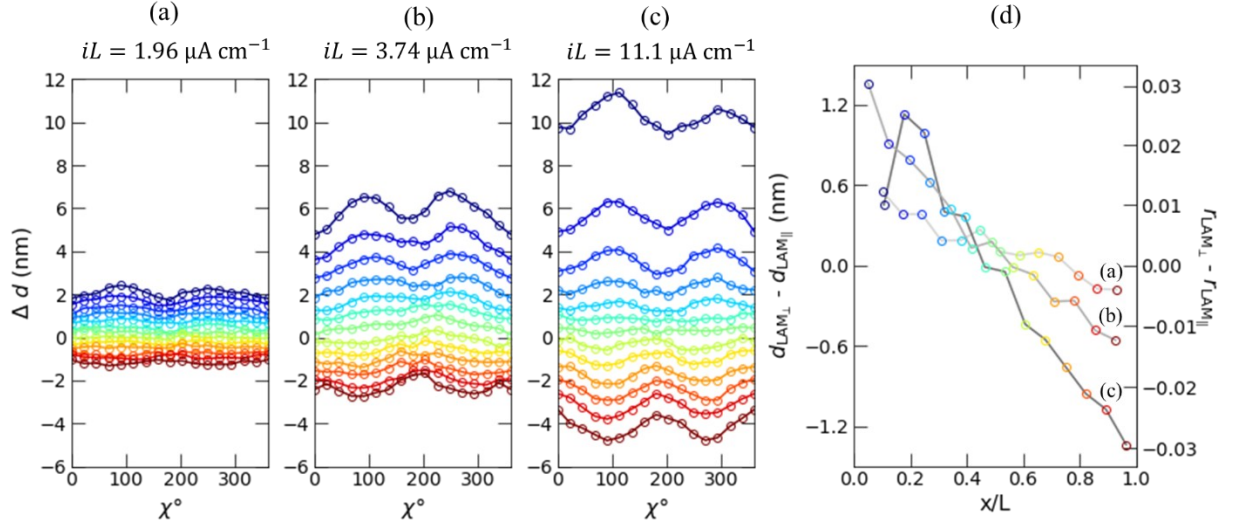
Figure 8. Orientation dependence of lamellar distortion. The change in domain spacing, Δd, defined by Eqn. 16 as a function of azimuthal angle, χ, is plotted for each cell position for the cell polarized at (a) $iL = 1.96$ µA cm⁻¹ at $t = 46.7$ h, (b) $iL = 3.74$ µA cm⁻¹ at $t = 46.7$ h, and (c) $iL = 11.1$ µA cm⁻¹ at $t = 60.7$ h. Each data set is based on the last scan taken at the end of each polarization. (d) Difference in domain spacing between $LAM_\perp$ and $LAM_{\parallel}$ as a function of normalized position, x/L, for the three data sets in (a), (b), and (c). The right axis is the

The local salt concentration within a single lamellar grain and domain spacing are intimately related. Thermodynamically, there is no reason why salt would prefer to reside in one grain over another based strictly on grain orientation relative to the current direction. We posit that the reason for preferential salt partitioning into perpendicular lamellae is related to the fact that the salt concentration gradient forms along the x-axis, independent of the local block copolymer grain structure (salt concentration gradients also develop along the x-axis in homopolymer electrolytes). Thus, there is force driving the lamellae to expand in the x-direction for regions near the positive electrode where $r > r_{avg}$ and contract in the x-direction for regions near the negative electrode where $r < r_{avg}$. This force naturally distorts lamellae which have PEO-PS interfaces oriented perpendicular to the x-axis (LAM). For lamellae with interfaces oriented parallel to the x-axis ($LAM_{¿∨¿¿}$), this force acts parallel to the PEO-PS interfaces, and therefore does not lead to additional lamellar distortions.

Conclusions

Concentrated solution theory provides a framework to predict the development of salt concentration gradients and the associated potential drop across the electrolyte when current is passed through a cell. This can be extended to predict the maximum current density which can be sustained through the electrolyte (*i.e.,* the limiting current, $i_{\lim ¿¿}$). The prediction is based on the condition that the salt concentration reaches zero at the negative electrode where lithium plating occurs. Experimentally, we find that the limiting current in SEO(19-20)/LiTFSI at $r = 0.16$ is approximately a factor of two lower than what is predicted from concentrated solution theory.

Small angle X-ray scattering performed on the electrolyte during dc polarization provides several key insights into the reasons for this observation. In particular, we use scattering data to track distortions of the block copolymer lamellae due to the passage of ionic current. The rearrangement of conducting and non-conducting domains is coupled to the observed limiting current: the passage of ionic current requires the lamellae to distort to accommodate the salt concentration gradient. Concentrated solution theory does not account for these effects.

The SAXS experiments show that that there was a net increase in the domain spacing of the block copolymer as the salt concentration gradient develops. We observed that grains with PS-PEO interfaces oriented perpendicular to the flow of ionic current ($LAM_{\perp}$) swell and contract to a greater extent compared to those with PS-PEO interfaces oriented parallel to the flow of ionic current ($LAM_{\parallel}$). It is obvious that $LAM_{\parallel}$ play an important role in ion transport as the conducting domains in these grains are parallel to the direction of macroscopic ion transport. Our work indicates that $LAM_{\perp}$ also play an important role. The formation of a salt concentration gradient that must arise due to ion transport across macroscopic length scales relies on the ability of the lamellae to swell and contract. These distortions occur to a greater extent in $LAM_{\perp}$. Both $LAM_{\parallel}$ and $LAM_{\perp}$ appear to be necessary to accommodate large ionic currents in block copolymer electrolytes.

AUTHOR INFORMATION

Corresponding Author

*E-mail: nbalsara@berkeley.edu

Notes

The authors declare no competing financial interest.

SUPPORTING INFORMATION

Supporting Information. Description of fits to 1D SAXS profiles, discussion of beam center correction, schematic and picture of experimental cell, experimental data and fits corresponding to Eqns. 3-6, example calculation of theoretical limiting current, cell mapping from SAXS transmission data, Nyquist plots from electrochemical cells used for SAXS experiments before

and after polarization, example SAXS peak fitting, additional domain spacing and orientation parameter data, calculation of lithium deposited at the negative electrode during polarization.

LIST OF SYMBOLS

Table 2.4 List of symbols and abbreviations

Symbol	Meaning
$\mathbf{A}$	electrode area (cm^2)
c	salt concentration (mol cm^{-3})
d	domain spacing (nm)
D	restricted diffusion coefficient of the salt (cm^2 s^{-1})
f	orientation parameter
F	Faraday constant (96485 C mol^{-1})
i	current density (μA cm^{-2})
I	current (μA)
$I(q)$	scattered X-ray intensity (a. u.)
$i_{\lim ¿ ¿}$	limiting current density (μA cm^{-2})
$i_{\lim ,expt}$	limiting current density measured by experiment (μA cm^{-2})
$i_{\lim ,theory}$	limiting current density predicted by theory (μA cm^{-2})
I_{ref}	max intensity of the primary scattering peak of the reference sample (a.u.)
I_s	scattered X-ray intensity (a. u.)
iL	current density normalized by the distance between electrodes (μA cm^{-1})
J_1	collection of terms integrated to obtain salt concentration gradients, defined by Eqn. 4
J_2	collection of terms integrated to obtain potential gradients, defined by Eqn. 6
L	distance between electrodes (cm)
LAM	lamellar morphology
$LAM_{¿ \vee ¿ ¿}$	lamellar morphology with PS/PEO interfaces oriented parallel to the current direction
LAM	lamellar morphology with PS/PEO interfaces oriented perpendicular to the current direction
$\mathbf{LiTFSI}$	lithium bis(trifluoromethanesulfonyl)imide
m	salt molality (mol kg^{-1})
M_i	molar mass of species i (g mol^{-1} or kg mol^{-1})
$\mathbf{PEEK}$	poly(ether ether ketone)
$\mathbf{PEO}$	poly(ethylene oxide)
$\mathbf{PS}$	polystyrene
q	scattering vector (nm^{-1})
$q^{¿}$	location of primary scattering peak (nm^{-1})
Q	integration of $q^2 I(q)$ over the primary scattering peak

r	molar ratio of lithium cations to ether oxygens in the electrolyte
R	universal gas constant (8.314 J mol^{-1} K^{-1})
r_{avg}	r averaged over the entire volume of electrolyte
R_b	bulk resistance of the electrolyte (Ω)
$R_{\int ii}$	electrolyte/electrode interfacial resistance (Ω)
SAXS	small angle X-ray scattering
SEO	polystyrene-block-polyethylene oxide
SEO(xx-yy)	SEO with xx kg mol^{-1} PS block and yy kg mol^{-1} PEO block
T	temperature (K)
t	time (s)
$t_{+ii^0 i}$	transference number of the cation with respect to the velocity of the solvent
U	potential drop across the electrolyte (V)
U_{ss}	potential drop across the electrolyte measured at steady state (V)
v_i	molar volume of species i (cm^3 mol^{-1})
x	axis parallel to current flow (see Fig. 3a)
x/L	normalized cell position
y	axis perpendicular to current flow and X-ray beam (see Fig. 3a)
z	axis parallel to the X-ray beam (see Fig. 3a)
z_i	charge number of species i
$Z_\Im$	imaginary component of impedance multiplied by A (Ω cm^2)
$Z_\Re$	real component of impedance multiplied by A (Ω cm^2)

GREEK

Symbol	Meaning
α	angle defining an azimuth on a 2D SAXS pattern (°)
Δd	difference in domain spacing at time t versus at $t = 0$ (nm)
ΔV	potential drop at the potentiostat leads (V)
$\Delta V_{\int ii}$	potential drop across the electrolyte/electrode interfaces (V)
κ	ionic conductivity (S cm^{-1})
v_i	number of species i that a salt dissociates into
ρ_{+ii}	current ratio obtained using i_Ω
ρ_c	conducting phase density (g cm^3)
ϕ_c	conducting phase volume fraction
χ	azimuthal angle on the 2D SAXS detector (°)

REFERENCES

(1)   Trahey, L.; Brushett, F. R.; Balsara, N. P.; Ceder, G.; Cheng, L.; Chiang, Y. M.; Hahn, N. T.; Ingram, B. J.; Minteer, S. D.; Moore, J. S.; Mueller, K. T.; Nazar, L. F.; Persson, K. A.; Siegel, D. J.; Xu, K.; Zavadil, K. R.; Srinivasan, V.; Crabtree, G. W. Energy Storage Emerging:

A Perspective from the Joint Center for Energy Storage Research. *Proc. Natl. Acad. Sci. U. S. A.* **2020**, 117 (*23*), 12550–12557.

(2)   Cheng, X.-B.; Zhang, R.; Zhao, C.-Z.; Zhang, Q. Toward Safe Lithium Metal Anode in Rechargeable Batteries: A Review. *Chem. Rev.* **2017**, 117 (*15*), 10403–10473.

(3)   Arya, A.; Sharma, A. L. A Glimpse on All-Solid-State Li-Ion Battery (ASSLIB) Performance Based on Novel Solid Polymer Electrolytes: A Topical Review. *J. Mater. Sci.* **2020**, 55 (*15*), 6242–6304.

(4)   Tu, Z.; Nath, P.; Lu, Y.; Tikekar, M. D.; Archer, L. A. Nanostructured Electrolytes for Stable Lithium Electrodeposition in Secondary Batteries. *Acc. Chem. Res.* **2015**, 48 (*11*), 2947–2956.

(5)   Isikli, S.; Ryan, K. M. Recent Advances in Solid-State Polymer Electrolytes and Innovative Ionic Liquids Based Polymer Electrolyte Systems. *Curr. Opin. Electrochem.* **2020**, *21,* 188–191.

(6)   Doyle, M.; Fuller, T. F.; Newman, J. The Importance of the Lithium Ion Transference Number in Lithium/Polymer Cells. *Electrochim. Acta* **1994**, 39 (*13*), 2073–2081.

(7)   Newman, J.; Balsara, N. P. *Electrochemical Systems*, 4th ed.; Wiley, **2021**.

(8)   Steinrück, H.-G.; Takacs, C. J.; Kim, H.-K.; Mackanic, D. G.; Holladay, B.; Cao, C.; Narayanan, S.; Dufresne, E. M.; Chushkin, Y.; Ruta, B.; Zontone, F.; Will, J.; Borodin, O.; Sinha, S. K.; Srinivasan, V.; Toney, M. F. Concentration and Velocity Profiles in a Polymeric Lithium-Ion Battery Electrolyte. *Energy Environ. Sci.* **2020**, *13*, 4312-4321.

(9)   Liu, J.; Monroe, C. W. Solute-Volume Effects in Electrolyte Transport. *Electrochim. Acta* **2014**, *135*, 447–460.

(10)   Nyman, A.; Behm, M.; Lindbergh, G. Electrochemical Characterisation and Modelling of the Mass Transport Phenomena in LiPF6-EC-EMC Electrolyte. *Electrochim. Acta* **2008**, 53 (*22*), 6356–6365.

(11)   Mullin, S. A.; Stone, G. M.; Teran, A. A.; Hallinan, D. T.; Hexemer, A.; Balsara, N. P. Current-Induced Formation of Gradient Crystals in Block Copolymer Electrolytes. *Nano Lett*. **2012**, 12 (*1*), 464–468.

(12)   Möhl, G. E.; Metwalli, E.; Müller-Buschbaum, P. In Operando Small-Angle X-Ray Scattering Investigation of Nanostructured Polymer Electrolyte for Lithium-Ion Batteries. *ACS Energy Lett.* **2018**, 3 (*7*), 1525–1530.

(13)   Galluzzo, M. D.; Loo, W. S.; Schaible, E.; Zhu, C.; Balsara, N. P. Dynamic Structure and Phase Behavior of a Block Copolymer Electrolyte under Dc Polarization. *ACS Appl. Mater. Interfaces* **2020**, 12 (*51*), 57421–57430.

(14)   Sharon, D.; Bennington, P.; Webb, M. A.; Deng, C.; De Pablo, J. J.; Patel, S. N.; Nealey, P. F. Molecular Level Differences in Ionic Solvation and Transport Behavior in Ethylene Oxide-Based Homopolymer and Block Copolymer Electrolytes. *J. Am. Chem. Soc.* **2021**, *143*, 3180–3190.

(15)   Shen, K.-H.; Brown, J. R.; Hall, L. M. Diffusion in Lamellae, Cylinders, and Double Gyroid Block Copolymer Nanostructures. *ACS Macro Lett.* **2018**, 7 (*9*), 1092–1098.

(16)   Villaluenga, I.; Pesko, D. M.; Timachova, K.; Feng, Z.; Newman, J.; Srinivasan, V.; Balsara, N. P. Negative Stefan-Maxwell Diffusion Coefficients and Complete Electrochemical Transport Characterization of Homopolymer and Block Copolymer Electrolytes. *J. Electrochem. Soc.* **2018**, 165 (*11*), A2766–A2773.

(17)   Singh, M.; Odusanya, O.; Wilmes, G. M.; Eitouni, H. B.; Gomez, E. D.; Patel, A. J.; Chen, V. L.; Park, M. J.; Fragouli, P.; Iatrou, H.; Hadjichristidis, N.; Cookson, D.; Balsara, N. P. Effect of Molecular Weight on the Mechanical and Electrical Properties of Block Copolymer Electrolytes. *Macromolecules* **2007**, 40 (*13*), 4578-4585.

(18)   Zhang, Z.; Krajniak, J.; Ganesan, V. A Multiscale Simulation Study of Influence of Morphology on Ion Transport in Block Copolymeric Ionic Liquids. *Macromolecules* **2021**, 54 (*11*) 4997-5010.

(19)   Delhorbe, V.; Bresser, D.; Mendil-Jakani, H.; Rannou, P.; Bernard, L.; Gutel, T.; Lyonnard, S.; Picard, L. Unveiling the Ion Conduction Mechanism in Imidazolium-Based Poly(Ionic Liquids): A Comprehensive Investigation of the Structure-to-Transport Interplay. *Macromolecules* **2017**, 50 (*11*), 4309-4321.

(20)   Sethuraman, V.; Mogurampelly, S.; Ganesan, V. Multiscale Simulations of Lamellar PS-PEO Block Copolymers Doped with LiPF$_6$ Ions. *Macromolecules* **2017**, 50 (*11*), 4542–4554.

(21)   Galluzzo, M. D. M. D.; Loo, W. S. W. S.; Wang, A. A. A. A.; Walton, A.; Maslyn, J. A. J. A.; Balsara, N. P. N. P. Measurement of Three Transport Coefficients and the Thermodynamic Factor in Block Copolymer Electrolytes with Different Morphologies. *J. Phys. Chem. B* **2020**, 124 (*5*), 921–935.

(22)   Teran, A. A.; Mullin, S. A.; Hallinan, D. T.; Balsara, N. P. Discontinuous Changes in Ionic Conductivity of a Block Copolymer Electrolyte through an Order–Disorder Transition. *ACS Macro Lett.* **2012**, 1 (*2*), 305–309.

(23)   Young, W.-S.; Epps, T. H. Ionic Conductivities of Block Copolymer Electrolytes with Various Conducting Pathways: Sample Preparation and Processing Considerations. *Macromolecules* **2012**, 45 (*11*), 4689–4697.

(24)   Irwin, M. T.; Hickey, R. J.; Xie, S.; So, S.; Bates, F. S.; Lodge, T. P. Structure-Conductivity Relationships in Ordered and Disordered Salt-Doped Diblock Copolymer/Homopolymer Blends. *Macromolecules* **2016**, 49 (*18*), 6928–6939.

(25)   Sharon, D.; Bennington, P.; Webb, M. A.; Deng, C.; De Pablo, J. J.; Patel, S. N.; Nealey, P. F. Molecular Level Differences in Ionic Solvation and Transport Behavior in Ethylene Oxide-Based Homopolymer and Block Copolymer Electrolytes. *J. Am. Chem. Soc.* **2021**, 143 (*8*), 3180–3190.

(26)   Kambe, Y.; Arges, C. G.; Czaplewski, D. A.; Dolejsi, M.; Krishnan, S.; Stoykovich, M. P.; De Pablo, J. J.; Nealey, P. F. Role of Defects in Ion Transport in Block Copolymer Electrolytes. *Nano Lett.* **2019**, 19 (*7*), 4684–4691.

(27)   Gribble, D. A.; Frenck, L.; Shah, D. B.; Maslyn, J. A.; Loo, W. S.; Mongcopa, K. I. S.; Pesko, D. M.; Balsara, N. P. Comparing Experimental Measurements of Limiting Current in Polymer Electrolytes with Theoretical Predictions. *J. Electrochem. Soc.* **2019**, 166 (*14*), A3228–A3234.

(28)   Maslyn, J. A.; Frenck, L.; Veeraraghavan, V. D.; Mu, A.; Ho, A. S.; Marwaha, N.; Loo, W. S.; Parkinson, D. Y.; Minor, A. M.; Balsara, N. P. Limiting Current in Nanostructured Block Copolymer Electrolytes. *Macromolecules* **2021**, 54 (*9*), 4010-4022.

(29)   Chu, K. T.; Bazant, M. Z. Electrochemical Thin Films at and above the Classical Limiting Current. *J. Appl. Math.* **2005**, 65 (*5*), 1485–1505.

(30)   Teran, A. A.; Balsara, N. P. Thermodynamics of Block Copolymers with and without Salt. *J. Phys. Chem. B* **2014**, 118 (*1*), 4–17.

(31)   Hadjichristidis, N.; Iatrou, H.; Pispas, S.; Pitsikalis, M. Anionic Polymerization: High Vacuum Techniques. *J. Polym. Sci. Part A Polym. Chem.* **2000**, 38 (*18*), 3211–3234.

(32)   Yuan, R.; Teran, A. A.; Gurevitch, I.; Mullin, S. A.; Wanakule, N. S.; Balsara, N. P. Ionic Conductivity of Low Molecular Weight Block Copolymer Electrolytes. *Macromolecules* **2013**, 46 (*3*), 914–921.

(33)   Hexemer, A.; Bras, W.; Glossinger, J.; Schaible, E.; Gann, E.; Kirian, R.; MacDowell, A.; Church, M.; Rude, B.; Padmore, H. A SAXS/WAXS/GISAXS Beamline with Multilayer Monochromator. *J. Phys. Conf. Ser.* **2010**, 247, 012007.

(34)   Kieffer, J.; Karkoulis, D. PyFAI, a Versatile Library for Azimuthal Regrouping. *J. Phys. Conf. Ser.* **2013**, 425, 202012.

(35)   Gomez, E. D.; Panday, A.; Feng, E. H.; Chen, V.; Stone, G. M.; Minor, A. M.; Kisielowski, C.; Downing, K. H.; Borodin, O.; Smith, G. D.; Balsara, N. P. Effect of Ion Distribution on Conductivity of Block Copolymer Electrolytes. *Nano Lett.* **2009**, 9 (*3*), 1212–1216.

(36)   Gilbert, J. B.; Luo, M.; Shelton, C. K.; Rubner, M. F.; Cohen, R. E.; Epps, T. H. Determination of Lithium-Ion Distributions in Nanostructured Block Polymer Electrolyte Thin Films by X-Ray Photoelectron Spectroscopy Depth Profiling. *ACS Nano* **2015**, 9 (*1*), 512–520.

(37)   Gartner, T. E.; Morris, M. A.; Shelton, C. K.; Dura, J. A.; Epps, T. H. Quantifying Lithium Salt and Polymer Density Distributions in Nanostructured Ion-Conducting Block Polymers. *Macromolecules* **2018**, 51 (*5*), 1917–1926.

(38)   Pesko, D. M.; Feng, Z.; Sawhney, S.; Newman, J.; Srinivasan, V.; Balsara, N. P. Comparing Cycling Characteristics of Symmetric Lithium-Polymer-Lithium Cells with Theoretical Predictions. *J. Electrochem. Soc.* **2018**, 165 (*13*), A3186–A3194.

(39)   Frenck, L.; Veeraraghavan, V. D.; Maslyn, J. A.; Müller, A.; Ho, A. S.; Loo, W. S.; Minor, A. M.; Balsara, N. P. Effect of Salt Concentration Profiles on Protrusion Growth in Lithium-Polymer-lithium Cells. *Solid State Ionics* **2020**, 358, 115517.

(40)   Pesko, D. M.; Timachova, K.; Bhattacharya, R.; Smith, M. C.; Villaluenga, I.; Newman, J.; Balsara, N. P. Negative Transference Numbers in Poly(Ethylene Oxide)-Based Electrolytes. *J. Electrochem. Soc.* **2017**, 164 (*11*), E3569–E3575.

(41)   Chintapalli, M.; Chen, X. C.; Thelen, J. L.; Teran, A. A.; Wang, X.; Garetz, B. A.; Balsara, N. P. Effect of Grain Size on the Ionic Conductivity of a Block Copolymer Electrolyte. *Macromolecules* **2014**, 47 (*15*), 5424–5431.

(42)   Chintapalli, M.; Le, T. N. P.; Venkatesan, N. R.; Mackay, N. G.; Rojas, A. A.; Thelen, J. L.; Chen, X. C.; Devaux, D.; Balsara, N. P. Structure and Ionic Conductivity of Polystyrene-Block -Poly(Ethylene Oxide) Electrolytes in the High Salt Concentration Limit. *Macromolecules* **2016**, 49 (*5*), 1770–1780.

(43)   Mongcopa, K. I. S.; Tyagi, M.; Mailoa, J. P.; Samsonidze, G.; Kozinsky, B.; Mullin, S. A.; Gribble, D. A.; Watanabe, H.; Balsara, N. P. Relationship between Segmental Dynamics Measured by Quasi-Elastic Neutron Scattering and Conductivity in Polymer Electrolytes. *ACS Macro Lett.* **2018**, 7 (*4*), 504–508.

(44)   Galluzzo, M. D.; Maslyn, J. A.; Shah, D. B.; Balsara, N. P. Ohm's Law for Ion Conduction in Lithium and beyond-Lithium Battery Electrolytes. *J. Chem. Phys.* **2019**, 151 (2), 020901.

(45)   Wang, H.; Newstein, M. C.; Krishnan, A.; Balsara, N. P.; Garetz, B. A.; Hammouda, B.; Krishnamoorti, R. Ordering Kinetics and Alignment of Block Copolymer Lamellae under Shear Flow. *Macromolecules 1999*, 32 (*11*), 3695–3711.

(46)   Kim, H.-K.; Balsara, N. P.; Srinivasan, V. Continuum Description of the Role of Negative Transference Numbers on Ion Motion in Polymer Electrolytes. *J. Electrochem. Soc.* **2020**, *167*, 110559.

(47)   Samuels, R. J. *Structured Polymer Properties*; Wiley, **1974**.

(48)   Wilkes, G. L. *Encyclopedia of Polymer Science and Engineering,* 2nd ed.; Wiley, **1988**.

(49)   White J. L. *Encyclopedia of Polymer Science and Engineering*, 2nd ed; Wiley, **1988**.

(50) Sax, J.; Ottino, J. M. Modeling of Transport of Small Molecules in Polymer Blends: Application of Effective Medium Theory. *Polym. Eng. Sci*. **1983**, 23, 165–176.